



Review

Sunlight-driven toluene photo-elimination using $\text{CeO}_2\text{-TiO}_2$ composite systems: A kinetic study

Mario J. Muñoz-Batista ^a, Anna Kubacka ^a, María Natividad Gómez-Cerezo ^{a,b},
David Tudela ^b, Marcos Fernández-García ^{a,*}

^a Instituto de Catálisis y Petroleoquímica, CSIC, C/Marie Curie, 2, 28049 Madrid, Spain

^b Departamento de Química Inorgánica, Facultad de Ciencias, Universidad Autónoma de Madrid, Campus Cantoblanco, 28049 Madrid, Spain

ARTICLE INFO

Article history:

Received 9 February 2013

Received in revised form 22 April 2013

Accepted 30 April 2013

Available online 9 May 2013

Keywords:

Toluene

Photocatalysis

Solar light

Photon absorption

Kinetics

ABSTRACT

A kinetic study of the behavior observed in the photocatalytic degradation of toluene under sunlight-type excitation and using composite $\text{CeO}_2\text{-TiO}_2$ catalysts is presented. The study focuses on analyzing kinetic differences within a series of composite catalysts with varying $\text{CeO}_2\text{:TiO}_2$ molar ratios. To this end, intrinsic expressions to represent the kinetics of toluene photo-degradation were derived from a proposed reaction scheme. These expressions explicitly included the effect of photon absorption on the reaction rate and lead to a mathematical expression of the reaction rate including two adjustable parameters. The modeling of the radiation field in the reactor was accomplished by numerically solving the radiative transfer equation. The radiation field and kinetic schemes were jointly used into a partial differential equation corresponding to the mass balance of toluene. The mathematical model was solved with an algorithmic based in the method of lines to deal with the partial differential equation, coupled with a nonlinear least-squares fitting algorithm to obtain kinetic parameter value estimations. Experimental runs for single oxide and composite $\text{CeO}_2\text{-TiO}_2$ catalysts were used for the fitting process. Good agreement was obtained between model predictions and experimental data, with a root mean square error below 0.65%. The kinetic behavior of composite samples with respect to the titania reference seems intimately related with the hole handling steps of the mechanism.

© 2013 Elsevier B.V. All rights reserved.

Contents

1. Introduction	627
2. Experimental	627
2.1. Catalyst preparation	627
2.2. Characterization details	628
2.3. Reaction system	628
3. Results and discussion	628
3.1. Modeling	628
3.1.1. Mass balance	628
3.1.2. Kinetic model	629
3.1.3. Radiation model	631
3.1.4. Numerical procedure	631
3.2. Experimental results	632
4. Conclusions	633
Acknowledgements	634
Appendix A. Obtaining integration limits of the radiation model	634
References	635

* Corresponding author. Tel.: +34915 85 4939; fax: +34 915 85 47 60.

E-mail addresses: mfg@icp.csic.es, m.fernandez@icp.csic.es (M. Fernández-García).

Nomenclature

N	total number of data points
t	time (s)
x	cartesian coordinate (m)
y	cartesian coordinate (m)
z	cartesian or cylindrical coordinate (m)
r	cylindrical coordinate (m)
R	inner radius reactor annulus (m)
R_{ext}	outer radius reactor annulus (m)
RL	lamp radius (m)
e	thickness (m)
η_G	unit vector outwardly directed normal to the catalytic film
v	axial velocity (m s^{-1})
D	molecular diffusivity coefficient ($\text{m}^2 \text{s}^{-1}$)
C	molar concentration (mol m^{-3})
r	superficial reaction rate ($\text{mol m}^{-2} \text{s}^{-1}$)
k	kinetic constant (units depend on the reaction step)
K	equilibrium adsorption constant ($\text{m}^3 \text{mol}^{-1}$)
$e^{a,s}$	local superficial rate of photon absorption (W m^{-2})
r_g	superficial rate of electron-hole generation ($\text{mol m}^{-2} \text{s}^{-1}$)
\mathbf{q}	local radiation flux vector (W cm^{-2})
q	local net radiation flux (W cm^{-2})
I	radiation intensity (W cm^{-2})
φ	spherical coordinate (rad)
θ	spherical coordinate (rad)
λ	wavelength (m)
α	kinetic parameters
ϕ	primary quantum yield ($\text{mol mol of photons}^{-1}$)
β	angle between the ray trajectory and the film outwardly directed normal (rad)
Ω	solid angle (sr)
κ	volumetric absorption coefficient (m^{-1})

Subscripts

0	initial condition
ads	adsorbed on the catalyst surface
min	minimum limiting value
max	maximum limiting value
λ	dependency on wavelength
dir	relative to the direct net radiative flux
ind	relative to the indirect net radiative flux
Ω	dependency on solid angle
L	relative to lamp
gl	relative to glass
s	relative to the sample film
exp	experimental value
mod	modeling result
lm	relative to the surface lamp

Special symbols

$[^*]$	concentration on the catalyst surface (mol m^{-2})
$\bar{*}$	denotes averaged value
$*$	denotes a vector

1. Introduction

Heterogeneous photocatalysis technology is considered as a promising route to afford pollutant degradation as well as hydrogen production processes. This is essentially based in the excellent performance and stability of titania (TiO_2), the most prominent photocatalytic material, for the mineralization of typical pollutants,

including refractory or non-biodegradable molecules, under mild conditions, e.g. room temperature and atmospheric pressure and using oxygen (air) as oxidant agent [1,2]. Nowadays, a significant research activity in this field is focused in the development of novel alternative materials to traditional TiO_2 capable to use of sunlight as the green energy source [3]. In this sense, the utilization of solar light as efficient as possible has been largely pursued. To achieve such framework objective, different strategies have been traditionally followed, based in all cases in the improvement of visible photon absorption. Among these, modification of TiO_2 by anion–cation (co)doping [3–12] or coupling TiO_2 with other semiconductors [3–19] displaying low band gaps (e.g. band gap energy in the visible light region) have proved to be viable ways to allow the use of visible photons in light to chemical conversion processes. Among composite systems with titania, cerium oxide appears as a perfect candidate due to several facts. First, ceria (CeO_2) itself is an active system under visible light [20–22]. In addition, ceria is a p -type semiconductor with potential adequate conduction/valence band positions to promote charge separation while in contact with anatase [3]. Such possibility has been previously exploited to obtain visible and/or sunlight-active composite photo-catalysts [23–25].

Here we focus on a kinetic study of the CeO_2 – TiO_2 system in the photo-elimination of toluene. Toluene photo-mineralization was chosen to test activity as it is thought to be an important constituent of anthropogenic emissions in urban atmospheres. Additionally, its photo-oxidation is a very demanding reaction and thus constitutes a tough chemical test to assess the potential of the TiO_2 -based systems in the photo-elimination of organic pollutants [26,27]. The mechanism and kinetics of toluene degradation has been the subject of a number of research works [28–31]. Most of the kinetic studies have employed Langmuir–Hinshelwood or simple mathematical-law (potential, exponential, etc.) type of kinetic expressions to represent the reaction rate. In such cases, model parameters are dependent on experimental conditions and cannot be easily extrapolated to the situations reported in other works. Only intrinsic kinetic data obtained from models that involve solution of the mass balances of the reacting species and the evaluation of the radiation field in the employed reactor can provide information valid for general use.

In the present work we propose an intrinsic expression for the photocatalytic degradation of toluene occurring in a gas-phase photo-reactor and employing a sunlight-type source. The kinetic equations are based on mechanistic steps discussed in the literature [28–31] and explicitly include the modeling of radiation absorption steps. The radiation field was evaluated by applying the radiative transfer equation to the heterogeneous systems [32]. In such way we can provide information with general validity for reactor design and scaling in the context of toluene photo-oxidation. The study also intends to shed some light in how CeO_2 affects the kinetic behavior of anatase TiO_2 . Results indicate that ceria alters significantly the hole-related radicals production/handling with respect to bare titania by effect of an intimate contact among titania and ceria phases.

2. Experimental

2.1. Catalyst preparation

Materials were obtained by means of a microemulsion preparation method utilizing *n*-heptane (Scharlau) as organic media, Triton X-100 (Aldrich) as surfactant and hexanol (Aldrich) as cosurfactant. A TiO_2 reference sample was obtained as a first step using a water in oil microemulsion and titanium tetraisopropoxide as precursor. In all composite samples and the CeO_2 reference, cerium nitrate (Alfa Aesar) was introduced in the aqueous phase

Table 1

Main characterization results of samples.

Sample	BET (m ² g ⁻¹)	Size (nm)		Pore volume (cm ³ g ⁻¹)	Pore size (nm)	Porosity (%)
		TiO ₂	CeO ₂			
TiO ₂	113.5	12.1	—	0.236	8.3	47.9
0.05CeO ₂ /TiO ₂	75.5	15.0	—	0.129	6.8	34.4
0.25CeO ₂ /TiO ₂	108.8	15.2	8.5	0.148	5.4	42.6

of a microemulsion. After stirring for 30 min, the stoichiometric (to obtain the corresponding Ce(III) hydroxide) quantity of tetramethylammonium-hydroxide (TMAH) was introduced from the aqueous phase of a similar microemulsion under stirring for ca. 5 min. For nanocomposite samples, a titanium tetraisopropoxide solution with isopropanol (2:3) was added dropwise on the Ce-containing microemulsion. Water/M (M = Ti, Ce, or Ce + Ti) and water/surfactant molar ratios were, respectively, 110 and 18 for all samples [33,34]. The resulting mixture was stirred for 24 h, centrifuged, and the separated solid precursors rinsed with methanol and dried at 110 °C for 12 h. After drying, the solid precursors were subjected to a heating ramp (2 °C min⁻¹) up to 500 °C, maintaining this temperature for 2 h. Samples names are TiO₂ or CeO₂ for the titania/ceria references, and xCeO₂/TiO₂ for the composite ones where x is the molar content of CeO₂ (in relation to a fixed amount of titania corresponding to 1 mol).

2.2. Characterization details

The BET surface areas and average pore volume and size were measured by nitrogen physisorption (Micromeritics ASAP 2010). XRD profiles were obtained with a Seifert D-500 diffractometer using Ni-filtered Cu K α radiation with a 0.02° step and fitted using the Von Dreele approach to the Le Bail method [35]; particle sizes were measured with XRD using the Williamson–Hall formalism [36]. Ce/Ti composition was analyzed by using inductively coupled plasma and atomic absorption (ICP-AAS; Perkin-Elmer, Optima 3300 DV). Changes from nominal x values reported in sample names were inferior to 6%. UV-vis transmission or diffuse reflectance spectroscopy experiments were performed with a Shimadzu UV2100 apparatus using, for diffuse experiments, BaSO₄ as reference. A summary of morphological and structural properties for all samples included in this work is presented in Table 1.

2.3. Reaction system

Gas phase selective photo-oxidation tests were carried out with toluene and using a set-up described in Fig. 1. The gas-phase photooxidation was tested in a continuous flow annular photoreactor containing ca. 40 mg of photocatalyst as a thin layer coating on a

pyrex tube. The corresponding amount of catalyst was suspended in 1 ml of ethanol, painted on a pyrex tube (cut off at ca. 290 nm) and dried at RT. The reacting mixture (100 cm³ min⁻¹) was prepared by injecting toluene (≥99%; Aldrich) into a wet (ca. 75% relative humidity, RH) 20 vol. % O₂/N₂ flow before entering to the photoreactor, yielding an organic inlet concentration of ca. 700 ppmv. Full experimental details are given in Table 2. After flowing the mixture for 6 h (control test) in the dark, the catalyst was irradiated by four fluorescent daylight lamps (6 W, Sylvania F6W/D), symmetrically positioned outside the photoreactor. The concentration of reactants and products was analyzed using an on-line gas chromatograph (Agilent GC 6890) equipped with HP-PLOT-Q/HP-Innowax columns (0.5/0.32 mm I.D. × 30 m) and TCD/FID detectors. 3 replicates of each experiment were used to obtain average values and errors of catalytic observables.

3. Results and discussion

3.1. Modeling

3.1.1. Mass balance

According to the photoreactor geometry (Fig. 1A/B), toluene mass balance follows the differential mass transfer Eq. (1) (presented in cylindrical coordinates), which is described in basic chemical engineering texts. The modeling of similar reactor geometries has been presented in previous studies [37–39]. In all these cases, the authors work under stationary conditions. This study is carried at non-stationary conditions and uses a heterogeneous three-dimensional model (Eq. (1)).

$$\frac{dC_{C_6H_5CH_3}}{dt} = \nu \frac{dC_{C_6H_5CH_3}}{dz} + D_{C_6H_5CH_3-Air} \left(\frac{d^2C_{C_6H_5CH_3}}{dr^2} + \frac{1}{r} \frac{dC_{C_6H_5CH_3}}{dr} \right) \quad (1)$$

This model has been obtained taking into account the following assumptions: (i) Newtonian fluid, (ii) unidirectional axial flow, (iii) azimuthal symmetry, (iv) constant physical properties, (v) negligible velocity profiles in r coordinate (relatively minor effects of this value in –time-dependent– toluene concentration behavior can be deduced from the mathematical expressions governing the flow [40] and the limited distance, 4 mm, between the coaxial cylinders; see Fig. 1), (vi) negligible axial diffusion when compared to the convective flux in that direction, (vii) constant diffusivity coefficient of the Toluene in the gas mixture ($D_{C_6H_5CH_3-Air} = 8.8 \times 10^{-6} \text{ m}^2 \text{ s}^{-1}$ [41]), and (viii) chemical reaction taking place only at the photocatalyst surface (negligible homogeneous photochemical reactions).

The numerical solution of Eq. (1), requires one initial condition in t, two boundary conditions in r and one boundary condition in z, Eqs. (2), (3), (4) and (5) respectively.

$$C_{C_6H_5CH_3}(r, z, t = 0) = C_{C_6H_5CH_3,0} \quad (2)$$

$$D_{C_6H_5CH_3-Air} \frac{dC_{C_6H_5CH_3}(r = R, z, t)}{dr} = -r_{C_6H_5CH_3} \quad (3)$$

Table 2

Reactor dimensions, characteristics and experimental operating conditions.

Reactor dimensions and characteristics	Lamp length (cm)	19
	Lamp radius (cm)	0.8
	Reactor length (cm)	15
	Reactor Inner radius (cm)	0.8
	Reactor Outer radius (cm)	1.2
	Radiation flux (mW cm ⁻²) ^a	1.2
	Nominal power (W)	6
	Emission range (nm)	290–745
Experimental operating conditions	Feed flow rate (cm ³ s ⁻¹)	1.67
	Temperature (°C)	25
	Pressure (Pa)	101,325
	Inlet Toluene concentration (mol cm ⁻³)	2.86E ⁻⁸
	Relative humidity (%)	75

^a Measured at center of reactor.

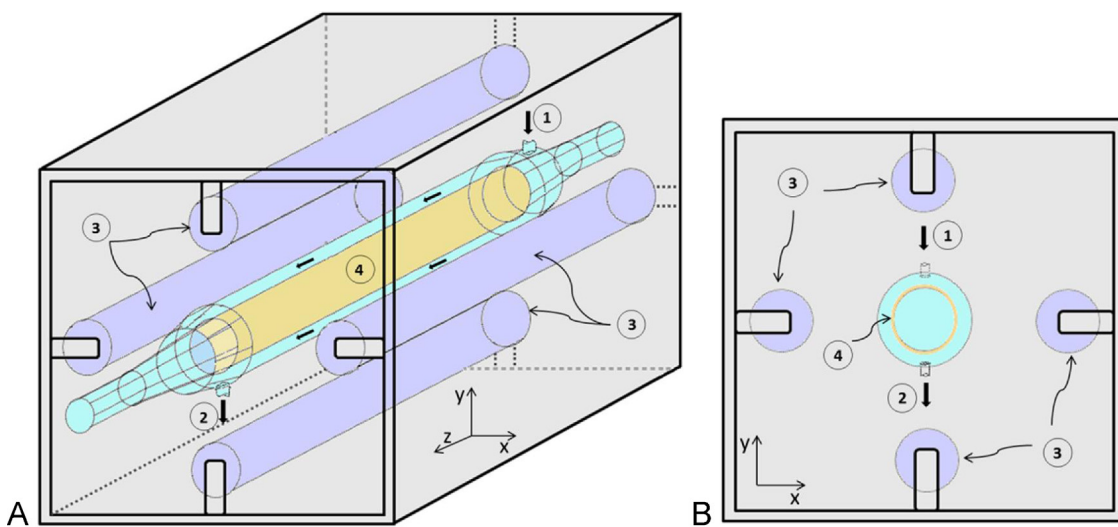


Fig. 1. (A) Photocatalytic annular reactor. (B) Side section view. (1) Gas inlet, (2) gas outlet, (3) sunlight-type lamp, (4) catalyst sample.

$$D_{C_6H_5CH_3-Air} \frac{dC_{C_6H_5CH_3}(r = R_{ext}, z, t)}{dr} = 0 \quad (4)$$

$$C_{C_6H_5CH_3}(r, z = 0, t) = C_{C_6H_5CH_3,0} \quad (5)$$

Note that Eq. (3) includes the reaction rate for toluene consumption.

3.1.2. Kinetic model

The expression of the intrinsic reaction kinetics was developed on the basis of the reaction scheme summarized in Table 3. This scheme is based on the well-established (initial) elemental steps of any photocatalytic processes: (i) the photo-excited sample generates electrons and holes, (ii) holes may react with adsorbed water and superficial OH⁻ ions to generate hydroxyl radicals, and (iii) molecular oxygen acts as an acceptor species in the electron-transfer reaction, partly reducing recombination processes and the resulting loss of energy as heat.

Also and according to the literature, (iv) the toluene molecule can be attacked by photogenerated holes (direct pathway) and hydroxyl radicals (indirect pathway) [28,31], generating in both cases, according to our experimental results, only a benzyl radical, (v) Benzyl radical can react then with oxygen to form a benzylperoxy radical [28–31], (vi) benzylperoxy radical can decompose thermally on the surface to give benzaldehyde and hydroxyl radical [30], and (vii) benzaldehyde can be further oxidized to benzoic acid which in turn decomposes on the sample surface via a photoKolbe mechanism [31]. Under the adopted experimental conditions, such a reaction scheme can be simplified by joining all organic

intermediates of the reaction in X_i and X_j ($X_{i,j}$), see Table 3 and Fig. 2. We also neglect the possible concentration of hydroxyl radical obtained in the step (vi) due to the limited significance of such production step in comparison with that occurring at the initial stage of the photo-process. According to the proposed reaction scheme, the rate of toluene photo-degradation is the sum of the degradation rates of the direct and indirect pathways:

$$r_{C_6H_5CH_3} = - (k_4[C_6H_5CH_3]_{ads}[\text{OH}^\bullet] + k_5[C_6H_5CH_3]_{ads}[\text{h}^+]) \quad (6)$$

The steady-state approximation may be applied to the net generation rates of free hydroxyl radical:

$$r_{\text{OH}^\bullet} = k_1[\text{H}_2\text{O}]_{ads}[\text{h}^+] - k_4[C_6H_5CH_3]_{ads}[\text{OH}^\bullet] - \sum k'_i[X_i]_{ads}[\text{OH}^\bullet] \approx 0 \quad (7)$$

From Eq. (7) we obtain:

$$[\text{OH}^\bullet] = \frac{k_1[\text{H}_2\text{O}]_{ads}[\text{h}^+]}{k_4[C_6H_5CH_3]_{ads} + \sum k'_i[X_i]_{ads}} \quad (8)$$

The steady-state approximation can be applied also to the holes reaction rate:

$$r_{\text{h}^+} = r_g - k_1[\text{H}_2\text{O}]_{ads}[\text{h}^+] - k_3[\text{h}^+][e^-] - k_5[C_6H_5CH_3]_{ads}[\text{h}^+] - \sum k''_i[X_i]_{ads}[\text{h}^+] \approx 0 \quad (9)$$

According to the results of Bahnemann et al. [42], applied also in previous kinetic studies [43], the Eq. (9) can be simplified considering that charge recombination in semiconductors is expected to be much faster than any chemically-related charge transfer step.

$$r_{\text{h}^+} = r_g - k_3[\text{h}^+][e^-] \approx 0 \quad (10)$$

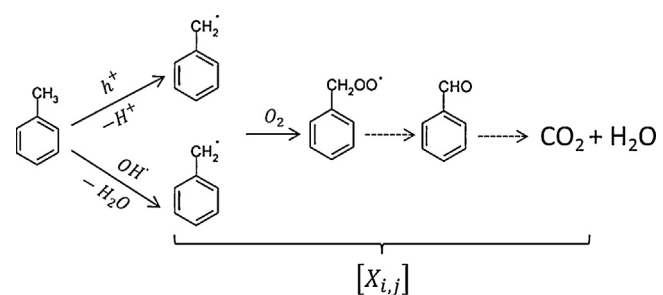


Fig. 2. Simplified diagram of the toluene degradation reactions.

Table 3
Simplified reaction scheme for the photocatalytic degradation of Toluene.

Reaction step	Reaction rate
$\text{Cat} + \lambda\gamma \xrightarrow{rg} \text{Cat} + \text{h}^+ + e^-$	r_g
$\text{h}^+ + \text{H}_2\text{O}_{ads} \xrightarrow{k_1} \text{OH}^\bullet + \text{H}^+$	$k_1[\text{H}_2\text{O}]_{ads}[\text{h}^+]$
$\text{h}^+ + \text{OH}_{ads} \xrightarrow{k_1} \text{OH}^\bullet$	$k_1[\text{OH}]_{ads}[\text{h}^+]$
$e^- + \text{O}_2_{ads} \xrightarrow{k_2} \text{O}_2^\bullet$	$k_2[\text{O}_2]_{ads}[e^-]$
$\text{h}^+ + e^- \xrightarrow{k_3} \text{heat}$	$k_3[\text{h}^+][e^-]$
$\text{C}_6\text{H}_5\text{CH}_3 \text{ads} + \text{OH}^\bullet \xrightarrow{k_4} X_i$	$k_4[\text{C}_6\text{H}_5\text{CH}_3]_{ads}[\text{h}^+]$
$\text{C}_6\text{H}_5\text{CH}_3 \text{ads} + \text{h}^+ \xrightarrow{k_5} X_i$	$k_5[\text{C}_6\text{H}_5\text{CH}_3]_{ads}[\text{h}^+]$
$X_{i,ads} + \text{OH}^\bullet \xrightarrow{k'_i} X_{j,ads}$	$k'_i[X_i]_{ads}[\text{OH}^\bullet]$
$X_{i,ads} + \text{h}^+ \xrightarrow{k''_i} X_{j,ads}$	$k''_i[X_i]_{ads}[\text{h}^+]$

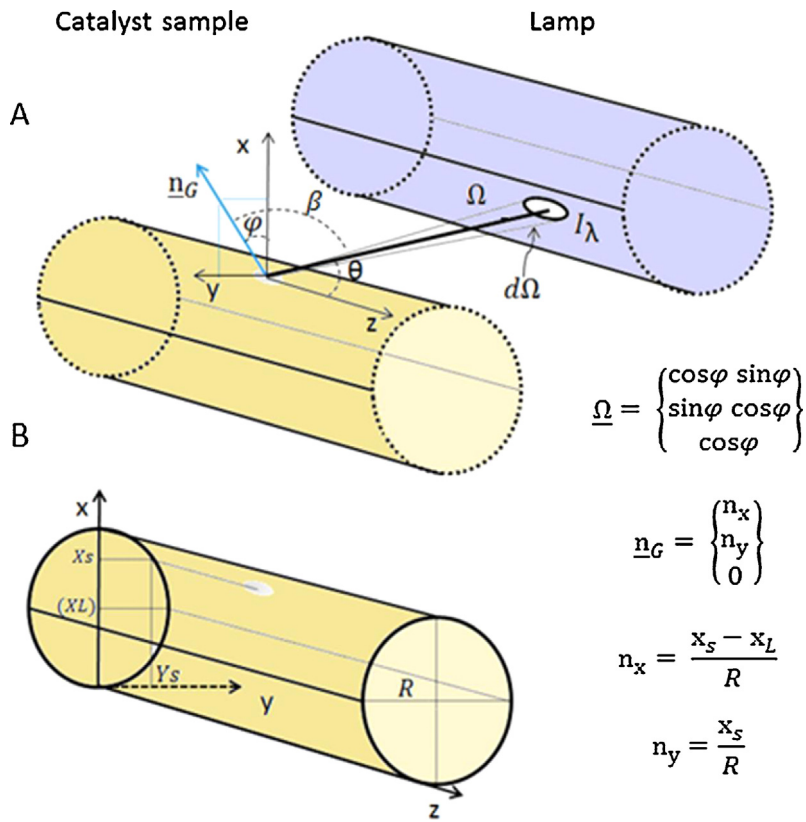


Fig. 3. (A) Coordinate system for the radiation model. (B) Coordinates of a point s_i located on the sample film.

Furthermore, under equilibrium conditions, the concentration of holes and electrons can be considered approximately equal and constant, then:

$$[h^+] = \sqrt{\frac{r_g}{k_3}} \quad (11)$$

Replacing Eqs. (11) and (8) into Eq. (6)

$$[H_2O]_{ads} = \frac{K_{H_2O} [Sites] C_{H_2O}}{1 + K_{C_6H_5CH_3} C_{C_6H_5CH_3} + K_{H_2O} C_{H_2O} + \sum K_{i,j} C_{X_{i,j}}} \quad (14)$$

$$\sum [X_{i,j}]_{ads} = \frac{\sum K_{i,j} [Sites] C_{X_{i,j}}}{1 + K_{C_6H_5CH_3} C_{C_6H_5CH_3} + K_{H_2O} C_{H_2O} + \sum K_{i,j} C_{X_{i,j}}} \quad (15)$$

Replacing Eqs. (13), (14) and (15) into Eq. (12)

$$\begin{aligned} r_{C_6H_5CH_3} = & -\sqrt{\frac{r_g}{k_3}} \left(\frac{k_4 K_{C_6H_5CH_3} [Sites] C_{C_6H_5CH_3} k_1 K_{H_2O} [Sites] C_{H_2O}}{(1 + K_{C_6H_5CH_3} C_{C_6H_5CH_3} + K_{H_2O} C_{H_2O} + \sum K_{i,j} C_{X_{i,j}}) (k_4 K_{C_6H_5CH_3} [Sites] C_{C_6H_5CH_3} + \sum k'_i K_i [Sites] C_{X_i})} \right. \\ & \left. + \frac{k_5 K_{C_6H_5CH_3} [Sites] C_{C_6H_5CH_3}}{(1 + K_{C_6H_5CH_3} C_{C_6H_5CH_3} + K_{H_2O} C_{H_2O} + \sum K_{i,j} C_{X_{i,j}})} \right) \end{aligned} \quad (16)$$

$$\begin{aligned} r_{C_6H_5CH_3} = & - \left(\sqrt{\frac{r_g}{k_3}} \left(\left(\frac{k_4 [C_6H_5CH_3]_{ads} k_1 [H_2O]_{ads}}{k_4 [C_6H_5CH_3]_{ads} + \sum k'_i [X_i]_{ads}} \right) \right. \right. \\ & \left. \left. + k_5 [C_6H_5CH_3]_{ads} \right) \right) \end{aligned} \quad (12)$$

The surface concentrations of adsorbed toluene, water and other reaction intermediates can be obtained from the balance of active sites. Assuming that toluene, water and other reaction intermediates compete for the same adsorption sites, the relation between the surface concentration and gas-phase concentrations is given by Eqs. (13), (14) and (15).

$$[C_6H_5CH_3]_{ads} = \frac{K_{C_6H_5CH_3} [Sites] C_{C_6H_5CH_3}}{1 + K_{C_6H_5CH_3} C_{C_6H_5CH_3} + K_{H_2O} C_{H_2O} + \sum K_{i,j} C_{X_{i,j}}} \quad (13)$$

In Eq. (16), under the adopted experimental conditions, the $\sum k'_i K_i [Sites] C_{X_i}$, $\sum K_{i,j} C_{X_{i,j}}$ terms can be neglected.

$$\begin{aligned} r_{C_6H_5CH_3} = & -\sqrt{\frac{r_g}{k_3}} \left(\frac{k_5 K_{C_6H_5CH_3} [Sites] C_{C_6H_5CH_3} + k_1 K_{H_2O} [Sites] C_{H_2O}}{(1 + K_{C_6H_5CH_3} C_{C_6H_5CH_3} + K_{H_2O} C_{H_2O} + \sum K_{i,j} C_{X_{i,j}})} \right) \end{aligned} \quad (17)$$

The local surface rate of electron–hole pair generation is given by Eq. (18), which assumes a wavelength averaged primary quantum yield.

$$r_g = \int_\lambda \phi_\lambda e_\lambda^{a,s}(x, y, z) d\lambda = \bar{\phi} \sum e_\lambda^{a,s}(x, y, z) \quad (18)$$

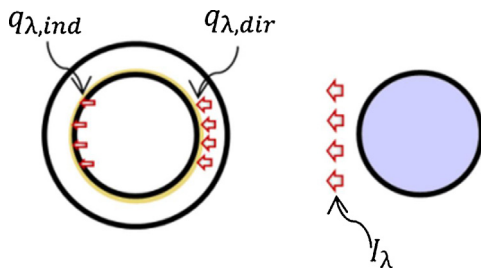


Fig. 4. Radiation fluxes scheme on the sample film.

Substituting Eq. (18) in Eq. (17), the toluene degradation rate can be expressed as:

$$r_{C_6H_5CH_3} = -\sqrt{e_{\lambda}^{a,s}} \left(\frac{\alpha_1 C_6H_5CH_3 + \alpha_2}{1 + K_{C_6H_5CH_3} C_6H_5CH_3 + K_{H_2O} C_{H_2O}} \right) \quad (20)$$

where the kinetic parameters α_1 and α_2 were defined by:

$$\alpha_1 = \sqrt{\frac{\bar{\phi}}{k_3}} k_5 K_{C_6H_5CH_3} [\text{Sites}] \quad (21)$$

$$\alpha_2 = \sqrt{\frac{\bar{\phi}}{k_3}} k_1 K_{H_2O} [\text{Sites}] C_{H_2O} \quad (22)$$

3.1.3. Radiation model

To evaluate Eq. (20) it is necessary to know the local superficial rate of photon absorption, $e_{\lambda}^{a,s}$. At each (x,y,z) position on the catalytic film the local superficial rate of photon absorption can be determined from Eq. (23).

$$e_{\lambda}^{a,s}(x, y, z) = q_{\lambda,dir}(x, y, z) + q_{\lambda,ind}(x, y, z) \quad (23)$$

where local net spectral radiation fluxes (direct or indirect; see Figs. 1A/B and 4) are defined as follows:

$$q_{\lambda}(x, y, z) = \eta_G \cdot q_{\lambda}(x, y, z) = \int_{\Omega} I_{\lambda}(x, y, z, \Omega) \Omega \cdot \eta_G d\Omega \quad (24)$$

The solution of this equation requires the representation of a three-dimensional light source assuming, in our case, the superficial emission model and using the ray-tracing method [37,44]. According to the coordinate system adopted (Fig. 3A), the coordinates of a point s_i located on the sample film (Fig. 3B), and the photo-reactor geometry, the radiation flux is given by Eq. (25).

$$q_{\lambda,L}(x, y, z) = \sum_{L=1}^{L=4} \sum_{\lambda} \int_{\varphi_{\min}}^{\varphi_{\max}} \int_{\theta_{\min}}^{\theta_{\max}} I_{\lambda,L} \sin^2 \varphi (n_x \cos \theta + n_y \sin \theta) d\varphi d\theta \quad (25)$$

The integration limits for the spherical coordinates φ and θ can be evaluated taking into account the geometry/dimensions of the reactor and the lamp (details in Appendix A).

Additionally, considering that air, toluene and water do not absorb radiation in the wavelength range of the lamp emission, we should take into account the light beam attenuation produced by the glass for the direct term and the system glass/sample/glass for the indirect term. Considering the sample, intensity will change due to three different causes: (a) part of the energy it carries will be scattered into other directions (out-scattering), (b) the intensity of a beam may be reinforced with the energy lost from other beams as scattered radiation (in-scattering), and (c) true energy absorption [44]. We will assume that scattered radiation is a small fraction of the total radiation that any beam is carrying at any point in the thin film, and after being scattered this energy is quickly lost to the radiation field due to true absorption and transformed into other

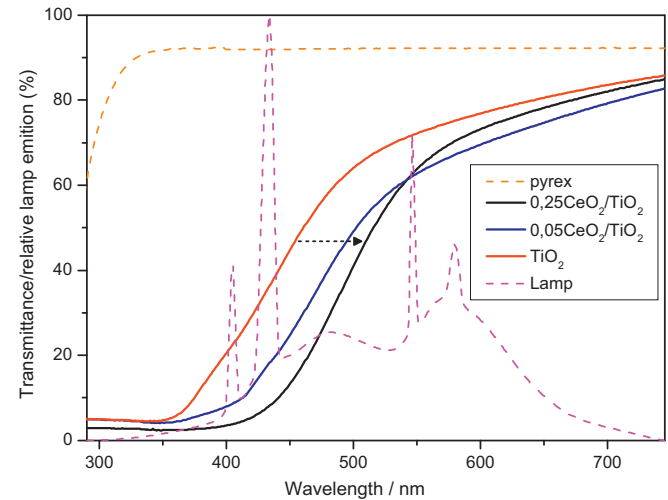


Fig. 5. Intensity distribution of the sunlight-type lamp and Transmittance of pyrex and samples.

forms of energy. While unequivocal justification of this assumption requires a full analysis of the optical properties of the catalyst under illumination at the experimental conditions used (not easy to carry out), we support the goodness of such hypothesis by calculation of the average angle between the ray and the catalyst surface in our lamp-catalyst experimental set-up (angle called beta in Fig. 3). Such angle is 59.2° , so it displays a value relatively reasonable for producing moderate reflection losses (minimization of reflection losses occurs when the angle between the ray and the normal to the catalyst surface is low). Therefore, true energy absorption would remain as the main factor of beam attenuation through our catalytic film. The final equation for the local superficial rate of photon absorption at each point (x,y,z) of the thin catalytic film is thus given by:

$$e_{\lambda}^{a,s}(x, y, z) = \sum_{L=1}^{L=4} \sum_{\lambda} \int_{\varphi_{\min}}^{\varphi_{\max}} \int_{\theta_{\min}}^{\theta_{\max}} I_{\lambda,L} \times \exp \left(-\frac{\kappa_{\lambda,gl} e_{gl}}{\cos \beta} \right) \times \left(1 - \exp \left(\frac{\kappa_{\lambda,s} e_s}{\cos \beta} \right) \right) \sin^2 \varphi (n_x \cos \theta + n_y \sin \theta) d\varphi d\theta + \sum_{L=1}^{L=4} \sum_{\lambda} \int_{\varphi_{\min}}^{\varphi_{\max}} \int_{\theta_{\min}}^{\theta_{\max}} I_{\lambda,L} \times \exp \left(-\frac{2\kappa_{\lambda,gl} e_{gl} - \kappa_{\lambda,s} e_s}{\cos \beta} \right) \times \left(1 - \exp \left(\frac{\kappa_{\lambda,s} e_s}{\cos \beta} \right) \right) \sin^2 \varphi (n_x \cos \theta + n_y \sin \theta) d\varphi d\theta \quad (26)$$

Values of $\kappa_{\lambda,gl} e_{gl}$ (glass) and $\kappa_{\lambda,s} e_s$ (for each sample), were determined from spectral transmittance measurements (Fig. 5).

3.1.4. Numerical procedure

First, a coordinate transformation (cartesian to cylindrical) in the local superficial rate of photon absorption was carried. This allows to express $e_{\lambda}^{a,s}$ in the natural coordinates of Eq. (1) (r,z). The mathematical model was solved with an algorithmic developed using MATLAB® R2010b. The algorithm uses a subroutine based in the method of lines (MOL [45]) to solve the partial differential Equation 1 (with backward substitution – t variable – to ensure solution stability-ode15s) subjected to conditions 2–5 and coupled with a nonlinear least-squares fitting algorithm (lsqnonlin, Algorithm: Trust-Region-Reflective Optimization [46]) to estimate the values and standard errors of the parameters included in Eq. (20). The termination tolerance on the function value was chosen to be E^{-12} . The accuracy and stability of the numerical solution of

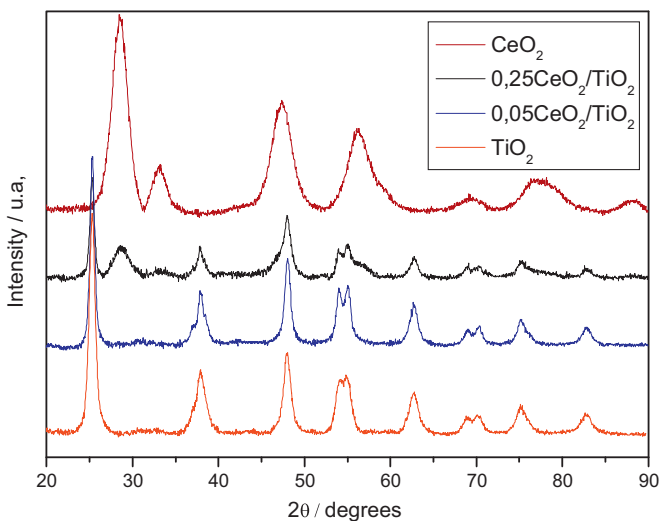


Fig. 6. XRD patterns of samples.

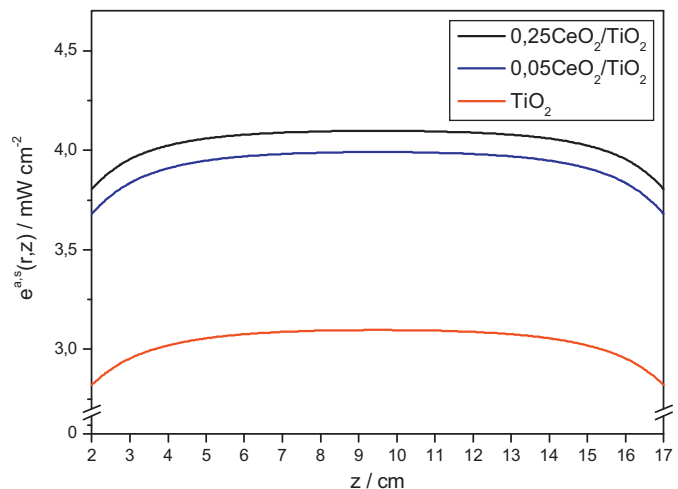
the MOL subroutine was investigated by changing the number of grid points for r , z , t variables and observing the effect on the output. From the results of the optimization algorithm it was found that, under the operating conditions of the experiments, the terms $K_{\text{H}_2\text{O}}\text{C}_{\text{H}_2\text{O}}$ and $K_{\text{C}_6\text{H}_5\text{CH}_3}\text{C}_{\text{C}_6\text{H}_5\text{CH}_3}$ were at least three orders of magnitude lower than 1, and thus could be neglected. A similar situation was encountered by Satuf et al. [47] in their time-dependent kinetic analysis of 4-chlorophenol photo-degradation. Considering this, the rates follow a first order kinetics with respect to the substrate concentration and can be defined as Eq. (27).

$$r_{\text{C}_6\text{H}_5\text{CH}_3} = -\sqrt{e_{\lambda}^{a,s}} (\alpha_1 \text{C}_6\text{H}_5\text{CH}_3 + \alpha_2) \quad (27)$$

Eq. (27) describes the reaction rate for toluene disappearance under the approximations (concerning both the gas and light-catalyst set-up experimental conditions as well as the toluene degradation mechanism) already described. As detailed in this section and the Supporting Information, this equation is developed to consider the time-dependence behavior observed in the toluene degradation at the initial stages of the reaction. Note that Eq. (27) has a double behavior; a first order kinetics in presence of toluene and a zero order kinetics in absence of the organic molecule. This result is inherent to the existence of two terms in Eq. (6), e.g. to consider toluene initial radical attack triggered by holes and OH^{\bullet} entities, together with the catalyst-surface-coverage-related simplifications (Eq. (17)) of the mathematical expression (Eq. (16)) derived from our reaction mechanism. As mentioned, such a procedure unavoidably leads to a non zero reaction rate in absence of toluene. The exact implications of this point will be further discussed below.

3.2. Experimental results

In Fig. 6 we plot the XRD patterns of TiO_2 and CeO_2 reference samples and $x\text{CeO}_2/\text{TiO}_2$ composites. The well known anatase (JCPDS card 78-2486, corresponding to the $I41\bar{a}$ space group) a fluorite (JCPDS card 87-0792, corresponding to the $Fm\bar{3}m$ space group) structures are observed, respectively, for the TiO_2 and CeO_2 references. Composite samples display the presence of the anatase phase but fluorite is only detected for the $0.25\text{CeO}_2/\text{TiO}_2$ sample. In these materials, anatase has a primary particle size of ca. 15 nm while fluorite, when detected, has a primary particle size of ca. 8.5 nm. The concomitant analysis of porosity (Table 1) indicates that for $0.05\text{CeO}_2/\text{TiO}_2$, small (XRD silent) CeO_x clusters are mainly

Fig. 7. Local rate of photon absorption profiles inside the reactor of samples as a function of the z coordinate.

located into anatase pores, partially occluding them. This justifies the change in porosity shown in Table 1. We also note the absence of significant anatase doping by ceria due to the constancy of the anatase cell volume (XRD derived cell volume is 136.3 and 136.4 Å for, respectively, TiO_2 and $0.05\text{CeO}_2/\text{TiO}_2$ samples), indicating that Ce is majorly at the surface of the anatase phase in this material. For $0.25\text{CeO}_2/\text{TiO}_2$ a significant part of ceria is forming fluorite-type particles with enough size to have a loose contact with titania. Such ceria nanoparticles generate a high surface area component, increasing this observable in the composite material as well as reversing the porosity trend detected for the sample with lower Ce content. This suggests that the non-contacting ceria nanoparticles correspond to the main Ce-containing component of the catalyst, which are responsible of the differential morphological characteristics with respect to the $0.05\text{CeO}_2/\text{TiO}_2$ specimen.

Optical properties and particularly photon absorption are of capital importance to interpret photo-catalytic behavior. Fig. 5 displays the UV-vis transmittance spectra of the materials which have (pseudo) band gap energies of 3.06 (TiO_2) 2.09 ($0.05\text{CeO}_2/\text{TiO}_2$) and 2.27 ($0.25\text{CeO}_2/\text{TiO}_2$) eV. The local superficial rate of photon absorption of the samples (at the photoreactor configuration) is displayed in Fig. 7. Fig. 7 plots along the z direction of the reactor (Fig. 1) show small (below 8%) and similar side-end effects for all samples. Additionally and as previously observed in Fig. 5,

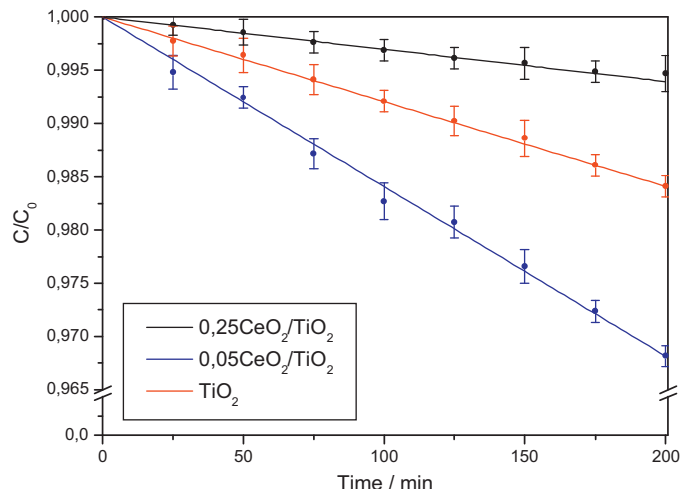


Fig. 8. Photocatalytic toluene disappearance experimental results and simulation.

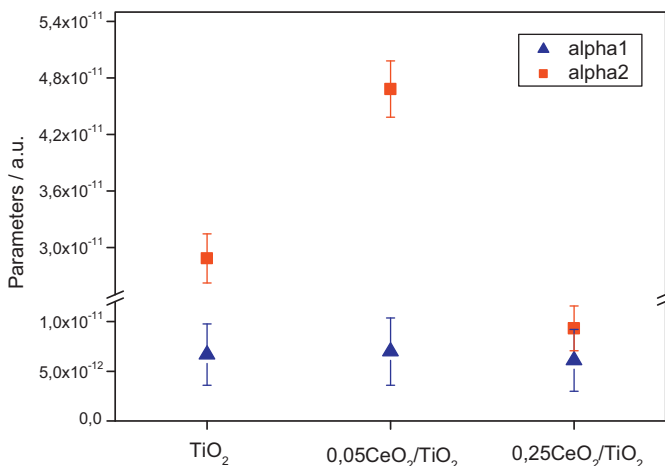


Fig. 9. Kinetic parameters for the TiO₂ reference and CeO₂/TiO₂ composite samples.

these profiles provide evidence that the presence of ceria, even at the lowest content tested, has a significant impact in the $e^{a,s}$ coefficient. Roughly, we observed an increase in $e^{a,s}$ coefficient of ca. 29 and 32% for, respectively, 0.05CeO₂/TiO₂ and 0.25CeO₂/TiO₂ samples. The enhancement of light absorption in presence of ceria is typically observed in the visible region [3,23–25] and may potentially affect positively the photo-activity of the material.

The beneficial effect of CeO₂ presence in nanocomposite catalysts is evident from the catalytic results presented in Fig. 8. However, not all xCeO₂/TiO₂ materials improve the performance of the titania reference, positive effects in toluene elimination activity being only observed for the 0.05CeO₂/TiO₂ sample. The kinetic analysis renders the parameter values presented in Fig. 9. Model prediction is a result of a complex calculation outlined in the previous Section 3.1. It should be here recalled that Eq. (27) was used as the kinetic expression, valid for the experimental working conditions. The quality of the model fit was evaluated with the root mean square error (RMSE) between the experimental value and the modeling described by Eq. 27.

$$\text{RMSE} = \sqrt{\frac{1}{N} \sum_1^N \left(\frac{C_{\text{C}_6\text{H}_5\text{CH}_3(\text{exp})} - C_{\text{C}_6\text{H}_5\text{CH}_3(\text{mod})}}{C_{\text{C}_6\text{H}_5\text{CH}_3(\text{exp})}} \right)^2} \times 100 \quad (28)$$

Note that our calculation consider a full analysis of the error including both the standard error observed in the toluene concentration or disappearance rate as well as the one related to the fitting procedure based in the minimization of the square of the differences between the model and the experiment. The RMSE was 0.65%, indicating the rather good description of the experimental data reached within the kinetic scheme here proposed. In brief, the small RMSE validates the goodness of our model and approach.

Another important issue about the kinetic model employed concerns the significance of the toluene zero order term included in Eq. (27). The importance of such term in our conditions is however secondary. As presented in Fig. S1 of the supporting information, even for reaction times at infinitum, the use of a constant concentration inlet infers that a zero toluene concentration is never reached. Thus, the region where the equation displays a zero order kinetics with respect to toluene is far from the one where experimental data are obtained and the kinetic behavior is subjected to analysis.

Values in Fig. 9 show a nearly constant (e.g. within experimental error) behavior for alpha1 parameter and a strong variation for alpha2 parameter. In the later case, we observed an increment with respect to the titania reference for the 0.05CeO₂/TiO₂ sample and a decrease for the 0.25CeO₂/TiO₂ sample. The photocatalytic

behavior as a function of the ceria content would be related to a combination of factors connected with the optical absorption as well as specific effects in some of the kinetic steps described in Table 3. The different behavior throughout of the series of alpha1, alpha2 parameters (see Eqs. (21) and (22)) suggests the relatively low importance of light absorption in the overall results. Moreover, the increase in surface photon absorption rate (Fig. 7) with respect to titania (1.29/1.32 for 0.05CeO₂/TiO₂/0.25CeO₂/TiO₂) does not correlate with the overall photo-catalytic behavior and, although it is a positive factor to achieve the maximum presented in Fig. 8 by the 0.05CeO₂/TiO₂ catalyst, it seems that it is not the key issue to explain photocatalytic behavior. The kinetic analysis has shown that ceria addition to the active anatase phase results in a positive/negative effect in alpha2 parameter, which may thus likely indicate a strong and direct influence in k_1 kinetic constant. This assumes that water interaction with the catalysts is relatively constant throughout the series as may be likely the case here where a high humidity level is used.

Ceria will thus optimize hole production by the composite system exclusively in presence of ceria entities with specific morphological characteristics. Thus, only in presence of small, XRD-silent entities a net overall positive effect in the kinetics of toluene photo-degradation is observed. The structural/electronic basis of such behavior is relatively complex of interpreting. We can speculate that the CeO₂-TiO₂ interface alters the production of hole-related radicals. To explain the different role of ceria as a function of the particle size we must first consider direct quantum size effects on band structure. Ceria is known to present a significant quantum size effect (QSE) on band gap. For samples with primary particle size above 10 nm QSE, first, locates band gap energy above the energy threshold characteristic of visible photons and, second, and more importantly, decreases significantly valence band position as to inhibit any efficient effect in hole handling [48,49]. However, as primary size decreases, the presence of Ce(III) is concomitantly observed. Depending on the concentration of Ce(III), the corresponding gap states can have a localized or band-type behavior, with potential different influence on charge separation. Therefore, Ce(III)-related (either Ce itself or the concomitant oxygen-vacancy states generates by charge neutrality in the ceria entities) would be responsible of visible light absorption and, more importantly, of having the adequate energy position for improving hole production in the composite materials. Similarly, this would also explain why the 0.25CeO₂/TiO₂ materials, which mainly presents fluorite nanoparticles having, according to the literature [48,49], very small quantities of Ce(III)-related localized states, may not improve hole production. Hole-related radical production/handling modification through contact between small ceria aggregates sited onto the anatase surface may thus be pointed out as the key issue to interpret the kinetic behavior of the CeO₂-TiO₂ materials under a daylight-type excitation.

4. Conclusions

A kinetic study of the time-dependent behavior observed in the photocatalytic degradation of toluene under sunlight-type excitation and using composite CeO₂-TiO₂ catalysts is presented. Such an approach was used to highlight differences within the composite series as well as with respect to the bare anatase reference. Intrinsic expressions to represent the kinetics of toluene photo-degradation were derived from a proposed reaction scheme. Such a scheme takes into account the attack of the organic by both OH[•] and hole radicals and leads to an expression with two adjustable parameters. A precise evaluation of the radiation field inside the reactor, required to model the effect of the radiation absorption on the reaction rate, was obtained by numerically solving the radiative

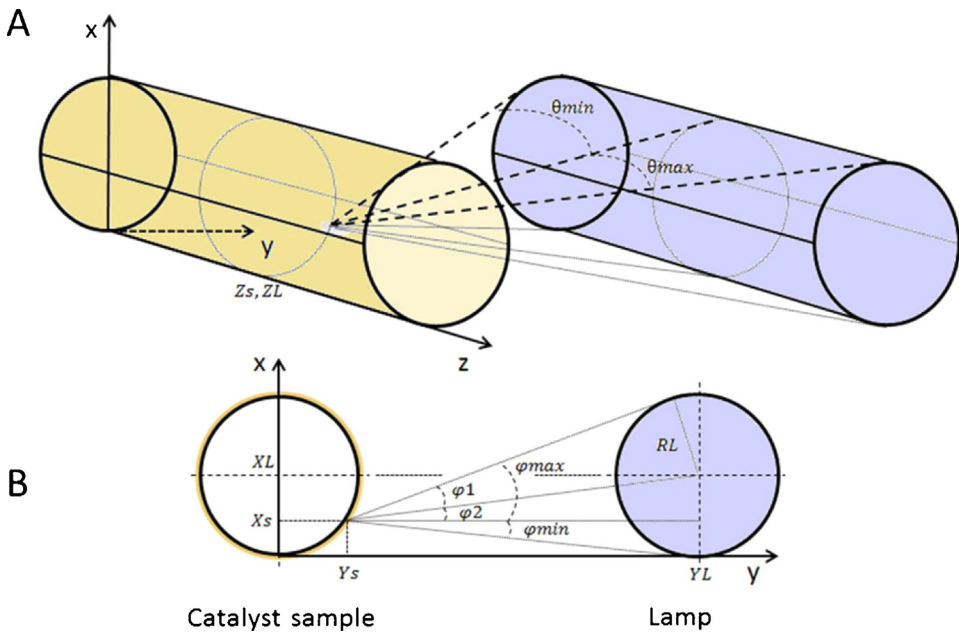


Fig. 10. (A) Coordinate system to define the integration limits (φ, θ) of radiation model. (B) x - y projection.

transfer equation. Subsequently, the time-dependent mass balance of toluene was solved with an algorithmic based in the method of lines to deal with the partial differential equation and coupled with a nonlinear least-squares fitting algorithm to obtain kinetic parameter value estimations.

The kinetic model successfully predicts the time evolution of toluene under operation conditions with a root mean square error below 0.65%. The values obtained for the two parameters indicate a kinetic behavior strongly dependent on the ceria loading on composite $\text{CeO}_2\text{-TiO}_2$ catalysts. The kinetic analysis supports that differential behavior of composite samples with respect to the titania reference would be intimately related with the hole-related radical production steps of the mechanism.

Acknowledgements

A. Kubacka and M.J. Muñoz-Batista thank MINECO for support thought, respectively, the postdoctoral "Ramón y Cajal" and predoctoral FPI programs. Financial support by MINECO is also acknowledged (project CTQ2010-14872/BQU).

Appendix A. Obtaining integration limits of the radiation model

For obtaining integration limits for Eq. (26), the following assumptions can be made: (i) the lamp is a perfect cylinder, (ii) the photon emitters are distributed uniformly on the lamp surface, (iii) each point of the lamp surface emits isotropically, and (iv) there are no changes in the direction or intensity of the rays when they leave the surface of the lamp [44]. Under such assumptions and using Fig. 10, phi limits are:

$$\varphi_{\max} = \varphi_1 + \varphi_2 \quad (29)$$

$$\varphi_{\min} = \varphi_1 - \varphi_2 \quad (30)$$

where:

$$\varphi_1 = \tan^{-1} \left(\frac{x_L - x_{s_i}}{y_L - y_{s_i}} \right) \quad (31)$$

$$\varphi_2 = \sin^{-1} \left(\frac{R_L}{\sqrt{(x_L - x_{s_i})^2 + (y_L - y_{s_i})^2}} \right) \quad (32)$$

Theta limits can be obtained (Fig. 10) from Eq. (33):

$$\cos \theta = \frac{\mathcal{Q} n_Z}{|\mathcal{Q}|} \quad (33)$$

where:

$$\mathcal{Q}_{\min} = \begin{Bmatrix} x_{Lm}(\varphi) - x_{s_i} \\ y_{Lm}(\varphi) - y_{s_i} \\ -z_{s_i} \end{Bmatrix} \quad (34)$$

$$\mathcal{Q}_{\max} = \begin{Bmatrix} x_{Lm}(\varphi) - x_{s_i} \\ y_{Lm}(\varphi) - y_{s_i} \\ z_L - z_{s_i} \end{Bmatrix} \quad (35)$$

$$\underline{n_Z} = \begin{Bmatrix} 0 \\ 0 \\ 1 \end{Bmatrix} \quad (36)$$

Solving this we can found

$$\theta_{\min}(\varphi) = \cos^{-1} \frac{-z_{s_i}}{\sqrt{(x_{Lm}(\varphi) - x_{s_i})^2 + (y_{Lm}(\varphi) - y_{s_i})^2 + z_{s_i}^2}} \quad (37)$$

$$\theta_{\max}(\varphi) = \cos^{-1} \frac{z_L - z_{s_i}}{\sqrt{(x_{Lm}(\varphi) - x_{s_i})^2 + (y_{Lm}(\varphi) - y_{s_i})^2 + z_{s_i}^2}} \quad (38)$$

where:

$$\begin{aligned} x_{Lm}(\varphi) &= x_L + (x_{s_i} - x_L) \cos \varphi^2 + (y_L - y_{s_i}) (\cos \varphi \sin \varphi) \\ &\quad - \sin \varphi \sqrt{(R_L^2 - (x_{s_i} - x_L) \cos \varphi + (y_L - y_{s_i}) \sin \varphi)^2} \end{aligned} \quad (39)$$

$$y_{Lm}(\varphi) = y_{s_i} + (y_L - y_{s_i}) \cos \varphi^2 + (x_{s_i} - x_L) (\cos \varphi \sin \varphi) \\ - \cos \varphi \sqrt{(RL^2 - (x_{s_i} - x_L) \cos \varphi + (y_L - y_{s_i}) \sin \varphi)^2} \quad (40)$$

References

- [1] M.R. Hoffmann, S.T. Martin, W. Choi, D.W. Bahnemann, *Chemical Reviews* 95 (1995) 69–96.
- [2] G. Colón, C. Belver, M. Fernández-García, in: M. Fernández-García, J.A. Rodríguez (Eds.), *Synthesis, Properties and Application of Oxide Nanoparticles*, Wiley, USA, 2007, ISBN: 978-0-471-72405-6 (Chapter 17).
- [3] A. Kubacka, M. Fernández-García, G. Colón, *Chemical Reviews* 112 (2012) 1555–1614.
- [4] Q. Li, R. Xie, E.A. Mintz, J.K. Shang, *Journal of the American Ceramic Society* 90 (2007) 3863–3868.
- [5] A. Kubacka, B. Bachiller-Baeza, G. Colón, M. Fernández-García, *Journal of Physical Chemistry C* 113 (2009) 8553.
- [6] A. Kubacka, B. Bachiller-Baeza, G. Colón, M. Fernández-García, *Applied Catalysis B* 93 (2010) 274–281.
- [7] A. Kubacka, G. Colón, M. Fernández-García, *Applied Catalysis B: Environmental* 95 (2010) 238–244.
- [8] T. Ohno, Z. Miyamoto, K. Nishijima, H. Kanemitsu, F. Xueyuan, *Applied Catalysis A* 302 (2006) 62–68.
- [9] J. Huán, S. Weng, J. Lin, *Journal of Natural Gas Chemistry* 4 (2012) 568–572.
- [10] H. Gao, B. Lu, F. Liu, Y. Liu, X. Zhao, *International Journal of Photoenergy* (2012) 453018, <http://dx.doi.org/10.1155/2012/453018>.
- [11] V. Menéndez-Flores, D.W. Bahnemann, T. Ohno, *Applied Catalysis B* 103 (2011) 99–108.
- [12] C.W. Lai, S. Sreekantan, *Journal of Alloys and Compounds* 547 (2013) 43–50.
- [13] M.C. Hidalgo, M. Maicu, J.A. Navío, G. Colón, *Journal of Physical Chemistry C* 113 (2009) 12840.
- [14] G. Colón, S. Murcia López, M.C. Hidalgo, J.A. Navío, *Chemical Communications* 46 (2010) 4809–4811.
- [15] A.M. Balu, B. Baruwati, E. Serrano, J. Cot, J. García-Martínez, R.S. Varma, R. Luque, *Green Chemistry* 13 (2011) 2750–2758.
- [16] N.K. Dey, M.J. Kim, K.-D. Kim, K.H. Lee, *Journal of Molecular Catalysis A* 337 (2011) 33–38.
- [17] X. Zhou, X. Li, Q. Zhao, S. Liu, *Journal of Colloid and Interface Science* 383 (2012) 13–18.
- [18] R.G. Nair, J.K. Roy, S.K. Samdarshi, A.K. Mukherjee, *Solar Energy Materials and Solar Cells* 105 (2012) 103–108.
- [19] A. Pérez-Larios, R. López, A. Hernández-Gordillo, F. Tzompantzi, R. Gómez, L.M. Torres-Guerra, *Fuel* 100 (2012) 139–143.
- [20] M.D. Hernández-Alonso, A.B. Hungría, A. Martínez-Arias, M. Fernández-García, J.M. Coronado, J.C. Conesa, J. Soria, *Applied Catalysis B* 50 (2004) 167–175.
- [21] M.D. Hernández-Alonso, A.B. Hungría, A. Martínez-Arias, J.M. Coronado, J.C. Conesa, J. Soria, M. Fernández-García, *Physical Chemistry Chemical Physics* 6 (2004) 3524–3529.
- [22] P. Ji, J. Zhang, F. Chen, M. Anpo, *Applied Catalysis B* 85 (2009) 148–154.
- [23] G. Li, D.Z. Zhang, J.C. Yu, *Physical Chemistry Chemical Physics* 11 (2009) 3775–3782.
- [24] H. Liu, M. Wang, Y. Wang, Y. Liang, W. Cao, Y. Su, *Journal of Photochemistry and Photobiology A* 233 (2011) 157–165.
- [25] Y. Wang, B. Li, C. Zhang, L. Cui, S. Kang, X. Li, L. Zhou, *Applied Catalysis B* 130–131 (2013) 277–284.
- [26] A. Fuerte, M.D. Hernández-Alonso, A.J. Maira, A. Martínez-Arias, M. Fernández-García, J.C. Conesa, J. Soria, *Chemical Communications* (2001) 2718–2719.
- [27] A. Fuerte, M.D. Hernández-Alonso, A.J. Maira, A. Martínez-Arias, M. Fernández-García, J.C. Conesa, J. Soria, *Journal of Catalysis* 212 (2002) 1–12.
- [28] O. d'Hennezel, P. Pichat, D.F. Ollis, *Journal of Photochemistry and Photobiology A* 118 (1998) 197–204.
- [29] V. Augugliaro, S. Coluccia, V. Loddo, L. Marchese, G. Martra, L. Palmisano, M. Schiavello, *Applied Catalysis B* 20 (1999) 15–27.
- [30] J.M. Coronado, J. Soria, *Catalysis Today* 123 (2007) 37–41.
- [31] M. Sleiman, P. Conchon, C. Ferronato, J.-M. Chovelon, *Applied Catalysis B* 86 (2009) 159–165.
- [32] A.E. Cassano, C.A. Martin, R.J. Brandi, O.M. Alfano, *Industrial and Engineering of Chemical Research* 34 (1995) 2155–2201.
- [33] P.G. De Gennes, C. Taupin, *Journal of Physical Chemistry* 86 (1982) 2294–2303.
- [34] M. Fernández-García, X. Wang, C. Belver, J.C. Hanson, J.A. Rodriguez, *Journal of Physical Chemistry C* 111 (2007) 674–682.
- [35] A. Le Bail, H. Duroy, J.L. Forquet, *Materials Research Bulletin* 23 (1988) 447–453.
- [36] G.K. Williamson, W.H. Hall, *Acta Metallurgica* 1 (1953) 22–31.
- [37] G.E. Imoberdorf, A.E. Cassano, O.M. Alfano, H.A. Irazoqui, *AIChE Journal* 52 (2006) 1814–1823.
- [38] G.E. Imoberdorf, A.E. Cassano, H.A. Irazoqui, O.M. Alfano, *Catalysis Today* 129 (2007) 118–126.
- [39] V. Tomašić, F. Jović, Z. Gomzi, *Catalysis Today* 137 (2008) 350–356.
- [40] R. Byron Bird, W.E. Stewart, E.N. Lightfoot, *Transport Phenomena*, second ed., John Wiley & Sons, New York, 2007.
- [41] R.H. Perry, C.H. Chilton (Eds.), *Chemical Engineer's Handbook*, fifth ed., McGraw-Hill, New York, 1973.
- [42] D.W. Bahnemann, M. Hilgendorff, R. Memming, *Journal of Physical Chemistry B* 101 (1997) 4265–4275.
- [43] G.L. Chiarello, D. Ferri, E. Sellì, *Journal of Catalysis* 280 (2011) 168–177.
- [44] G.E. Imoberdorf, H.A. Irazoqui, A.E. Cassano, O.M. Alfano, *Industrial and Engineering Chemistry Research* 44 (2005) 6075–6085.
- [45] I. Danaila, P. Joly, S.K. Kaber, M. Postel, *Numerical approximation of Partial Differential Equations*, Springer, Berlin, 2006.
- [46] T.F. Coleman, Y. Li, *SIAM Journal on Optimization* 6 (1994) 418–445, references therein.
- [47] M.L. Satuf, R.J. Brandi, A.E. Cassano, O.M. Alfano, *Applied Catalysis B* 82 (2008) 37–49.
- [48] M. Fernández-García, A. Martínez-Arias, J.C. Hanson, J.A. Rodríguez, *Chemical Reviews* 104 (2004) 4063–4104.
- [49] S. Tsunekawa, J.T. Wang, Y. Kawazoe, *Journal of Alloys and Compounds* 408–4012 (2006) 1145–1148.